PNAS RESEARCH ARTICLE | EARTH, ATMOSPHERIC, AND PLANETARY SCIENCES

Matrix effects reshape organic aerosol volatility and atmospheric persistence

Qiaorong Xie[a], Abigail M. Smith[a], Sara C. Botero-Carrizosa[a], Steven A. L. Sharpe[a], Gali Dekel[b], Nicole A. June[c], Manish Shrivastava[c], Yuqing Dai[d], Kevin Ridgway[e], Christian L'Orange[e], Shantanu H. Jathar[e], Katherine S. Hopstock[f], Sergey A. Nizkorodov[f], Yinon Rudich[g], and Alexander Laskin[a,h,1]

Affiliations are included on p. 6.

Edited by Mark Howard Thiemens, University of California, San Diego, La Jolla, CA; received April 30, 2026; accepted June 19, 2026

The volatility of individual species is a fundamental property governing the gas-particle partitioning of organic aerosols. However, in complex organic mixtures, a compound's apparent volatility may differ from its intrinsic volatility, depending on the matrix's chemical composition. Herein, we systematically investigate component-resolved, mixture-specific volatility for more than 1,500 individual species across 33 proxies and chemically complex mixtures representative of selected organic aerosol types. The results show that species in simplified proxies and reference mixtures with limited components follow a higher-volatility trend that approaches their intrinsic values, whereas species present in ambient and biomass-burning organic aerosols exhibit the opposite behavior, with systematically reduced apparent volatility attributable to matrix effects. Using levoglucosan (LG), a representative biomass-burning tracer, as an illustrative example, we find that its volatility in complex organic mixtures is reduced by 1 to 4 orders of magnitude relative to its intrinsic volatility in pure LG. This pronounced reduction underscores strong matrix effects that substantially suppress the apparent volatility of individual species in mixed systems. Machine-learning analysis further indicates that mixture-dependent molecular metrics are more predictive of apparent volatility than compound-specific molecular properties that define intrinsic volatility. Collectively, these findings highlight the critical role of intermolecular interactions in governing gas-particle partitioning in multicomponent systems. This study provides strong evidence that matrix effects significantly influence the apparent volatility of individual species in aerosols and other environmental organic mixtures and should be explicitly considered in volatility prediction frameworks and aerosol transport models.

intrinsic and apparent volatility | organic aerosol | matrix effects | complex mixtures | atmospheric persistence; levoglucosan

Significance

Matrix effects in chemically complex organic aerosol (OA) mixtures markedly suppress the apparent volatility of individual species, causing substantial deviations from intrinsic, pure-compound-based volatility assumptions. When implemented in chemical transport modeling, these reduced volatilities lead to large increases in predicted biomass-burning OA mass loadings, extended atmospheric lifetimes, and enhanced regional transport. The results demonstrate that neglecting matrix effects can systematically underestimate OA burdens and their climate and air-quality impacts. Incorporating mixture-dependent volatility parameterizations is therefore essential for improving predictions by regional and global atmospheric models.

Organic aerosols (OA) are widespread in the atmosphere. They are commonly distinguished as primary organic aerosol (POA) emitted directly mostly from wildfires and anthropogenic sources (1–3), and secondary organic aerosol (SOA), formed when volatile organic compounds (VOCs) oxidize and their products partition into the particle phase (3–5). In reality, these categories rapidly blur as gases and particles age, creating complex OA mixtures whose composition and properties (molecular weight, structure, oxidation state, volatility, light absorption, and reactivity) evolve with time (6–9). Multiphase physicochemical processes such as condensation, evaporation, coagulation, cloud processing, heterogeneous surface reactions, water uptake, and aqueous-phase chemistry further modify OA during atmospheric transport (10–13). Environmental drivers such as solar radiation, oxidant levels, humidity, temperature, and pressure strongly modulate these pathways, altering particle properties and their roles in atmospheric processes and air quality (14).

Atmospheric organic species exist in a dynamic equilibrium between their gas and condensed (particle) phases (14). The saturation vapor pressure (P_T, Pa) of these species, which is often expressed as saturation gas-phase mass concentration (C_T, $\mu g \cdot m^{-3}$) or volatility, is a fundamental property governing temperature- and pressure-dependent gas-particle partitioning. Volatility strongly influences the atmospheric fate of organic species (15, 16), impacts OA formation and aging (17–19), and is therefore critical for modeling OA transformations (20–23). The volatility of OA species depends on their intrinsic chemical properties, such as elemental composition, polarity and molecular structures, as well as on intermolecular interactions within complex mixtures and external environmental conditions, including temperature, pressure, relative humidity, and total organic mass loading (24–31). Representing OA volatility in models remains challenging

Author contributions: Q.X. and A.L. designed research; Q.X., A.M.S., S.C.B.-C., S.A.L.S., and K.S.H. performed research; G.D., N.A.J., M.S., Y.D., K.R., C.L., and S.H.J. contributed new reagents/analytic tools; Q.X., A.M.S., S.C.B.-C., S.A.N., Y.R., and A.L. analyzed data; Q.X., S.A.L.S., and K.R. collected samples; and Q.X. and A.L. wrote the paper.

The authors declare no competing interest.

This article is a PNAS Direct Submission.

[1]To whom correspondence may be addressed. Email: alaskin@purdue.edu.

This article contains supporting information online at https://www.pnas.org/lookup/suppl/doi:10.1073/pnas.2614944123/-/DCSupplemental.

Published July 22, 2026.

because apparent (effective) gas-particle partitioning in real-world mixtures is governed not only by the compound-specific properties but is further shaped by matrix interactions among coexisting organics. The volatility basis set (VBS) provides a useful framework for tackling this complexity (32). Various experimental and modeling approaches, such as tandem differential mobility analyzers (33), aerosol and chemical ionization mass spectrometers (34), and molecular corridor estimations (35), have been employed to infer VBS distributions. Nonetheless, these methods still face challenges in directly measuring the volatility of OA components in real atmospheric systems due to their chemical complexity, nonideal behavior, and transport limitations.

Recent experimental advancements have significantly improved the chemical characterization and measurement of apparent, component-specific volatility of OA species using a method that couples temperature-programmed desorption (TPD) with direct analysis in real time (DART) ionization and high-resolution mass spectrometry (HRMS) (36, 37). This approach provides high-resolution molecular formulas for individual OA constituents together with direct volatility measurements, enabling quantification of gas-particle partitioning and constraining key bulk properties of OA mixtures, including glass transition temperature and viscosity (37–40). The method and the associated data analysis framework have been validated across diverse systems, including biogenic SOA mixtures (37, 39), biomass burning organic aerosol (BBOA) (38), and ambient urban OA (40), and demonstrate a close agreement with earlier experimental findings (41–50). For each characterized OA component (i), the apparent volatility ($^{i}C^{*}_{T}$, $\mu g \cdot m^{-3}$) is determined across a broad temperature (T) range, reported as paired values of condensed-to-gas phase transition enthalpy ($^{i}\Delta H^{*}$, $kJ \cdot mol^{-1}$) and reference saturation mass concentration at 298 K ($^{i}C^{*}_{298\,K}$, $\mu g \cdot m^{-3}$). These two parameters define effective $^{i}C^{*}_{T}$ values through the Clausius–Clapeyron and the ideal gas law equations. The volatility characteristics of individual components in different mixtures are then used to establish semiempirical correlations between $^{i}\Delta H^{*}$ and $\log(^{i}C^{*}_{298\,K})$ yielding mixture-specific parameterizations practical for modeling (40).

Here, we compile component-resolved, mixture-dependent volatility measurements for >1,500 individual species across >30 distinct OA mixtures, enabling a comparison between simplified proxies and chemically complex ambient samples (*SI Appendix*, Supplemental Note 1). Simplified biogenic OA proxies and reference mixtures of few components generally align with a higher-volatility trend (37, 49), that has served as the basis for models predicting volatility of individual organic species (51, 52). In contrast, ambient OA and BBOA mixtures deviate markedly from this behavior, exhibiting systematically reduced volatility attributable to matrix effects, driven by nonideal, composition-dependent intermolecular interactions in multicomponent mixtures, which can be described thermodynamically in terms of composition-dependent activity coefficient (40, 48, 50).

Results and Discussion

Fig. 1 shows a plot of the thermodynamically coupled $^{i}\Delta H^{*}$ vs. $\log(^{i}C^{*}_{298\,K})$ values, compiled from individual species (i) detected and characterized across the full set of OA mixtures (*SI Appendix*, Table S1). Substantial overlap is observed among the datasets from different mixture types. For improved visualization of mixture-specific patterns, the same data are also presented in *SI Appendix*, Fig. S1 as 12 separate panels, each displaying a subdivision of the dataset by mixture type. The plots show that individual compounds

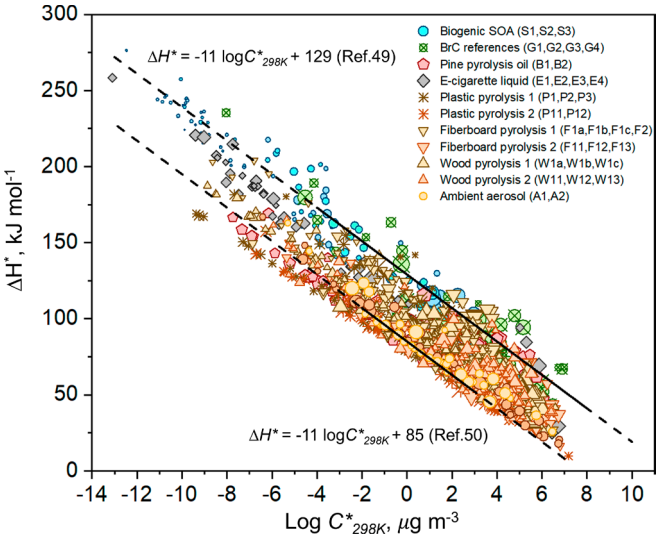

Fig. 1. Relationship between the apparent values of ($^{i}\Delta H^{*}$) and $\log^{i}C^{*}_{298\,K}$ for individual species measured across distinct OA mixtures representative of various emission sources. The upper and lower lines correspond to the trends reported for biogenic OA by Epstein et al. (49) and anthropogenic OA reported by Ranjan et al. (50) respectively. Solid line segments indicate the ranges over which original experimental values were reported, while dashed lines show extrapolations beyond those ranges. Marker size is scaled to the cube root of the corresponding mass spectral peak intensities to reflect relative abundance. Each data point represents an elemental formula-resolved feature and may include contributions from unresolved structural isomers associated with the same elemental composition

generally fall within a broad corridor approximately limited by the lower and upper volatility trend lines corresponding to biogenic OA with $^{i}\Delta H^{*} = -11 \times \log^{i}C^{*}_{298\,K} + 129$ and anthropogenic OA with $^{i}\Delta H^{*} = -11 \times \log^{i}C^{*}_{298\,K} + 85$, as reported in the literature (49, 50). However, the position of each mixture between these two lines depends strongly on its composition and source type. Within individual mixtures, $^{i}\Delta H^{*}$ and $\log(^{i}C^{*}_{298\,K})$ values follow an overall linear trend, but the mixture-specific slopes and intercepts differ, reflecting the combined effects of composition-dependent entropy variations, nonideal mixing, and matrix interactions (*SI Appendix*, Supplemental Note 2). Datasets corresponding to BrC references (G mixtures) composed of a few selected reference compounds and laboratory-generated biogenic OA proxies (S mixtures) cluster near the upper trend line, indicating higher effective volatility. In contrast, mixtures with greater compositional complexity and molecular diversity tend to cluster closer to the lower trend line, reflecting systematically lower apparent volatility. These include ambient OA (A mixtures), biomass-burning OA (B mixtures), and OA mixtures collected from pyrolysis tests with construction wood, fiberboard, and plastic materials (most W, F, and P mixtures). A subset of W, F, and P mixtures, as well as e-cigarette OA (E mixtures), occupy an intermediate region between the upper and lower limiting trends. This downward shift observed in compositionally diverse OA mixtures reflects pronounced matrix effects and nonuniform entropy contributions to the volatilization of individual components (*SI Appendix*, Figs. S2 and S3), whereby intermolecular interactions stabilize the condensed-phase species and suppress their evaporation.

Fig. 2 further illustrates matrix-induced volatility suppression based on the mixture specific measurements of levoglucosan (LG) evaporation, a widely used tracer of biomass burning emissions (53, 54). The apparent values of $^{LG}\Delta H^{*}$ and $\log(^{LG}C^{*}_{298\,K})$ derived from Arrhenius plots of LG in a pure single-component reference sample and complex mixtures vary substantially, as shown in Fig. 2*A* and elaborated in *SI Appendix*, Fig. S4. These differences

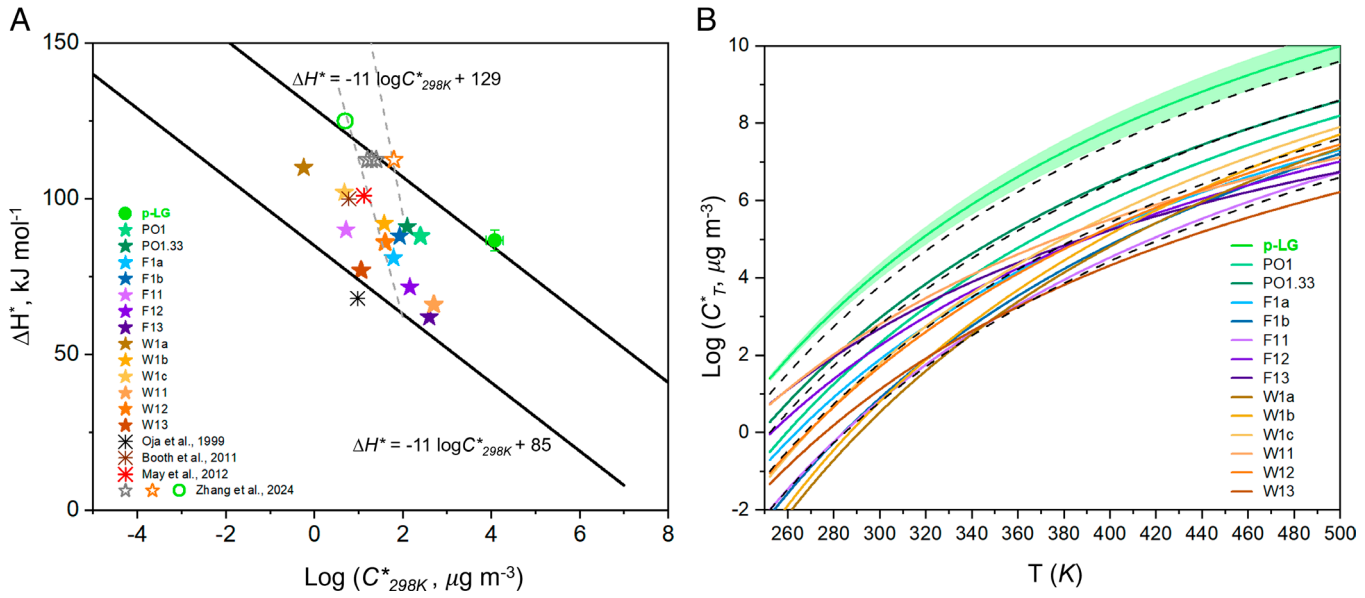

Fig. 2. (*A*) Apparent values of ${}^{LG}\Delta H^*$ and $\log({}^{LG}C^*_{298\,K})$ for levoglucosan (LG) reported in this study across multiple OA mixtures, together with measurements for pure levoglucosan (p-LG) samples and additional literature data. Solid symbols denote measurements from this work, while open symbols represent literature-reported experimental values (56–58). The upper and lower solid lines correspond to the ΔH^* vs. $\log(C^*_{298\,K})$ relationships reported by Epstein et al. (49) and Ranjan et al. (50), respectively. Dashed lines indicate trends reported by Zhang et al. (55) based on measurements of aerosolized particles. (*B*) Temperature-dependent $\log({}^{LG}C^*_T)$ values calculated using the parameters shown in (*A*). Dashed gray lines indicate unit intervals in $\log(C^*_T)$ to facilitate visual comparison. In both panels, bright green symbols and colored curves represent p-LG measurements and calculations. Together, these results demonstrate that matrix effects substantially suppress LG volatility in complex organic mixtures relative to its behavior as a pure compound.

indicate that the evaporation behavior of LG depends strongly on the surrounding mixture, reflecting pronounced matrix effects that modify the evaporation process within multicomponent systems. Fig. 2*A* compares the apparent ${}^{LG}\Delta H^*$ and $\log({}^{LG}C^*_{298\,K})$ values measured for pure levoglucosan (p-LG) with those obtained for LG present in B, W, and F mixtures generated from pyrolysis emissions (*SI Appendix*, Table S1). Notably, the p-LG measurements are highly reproducible (*SI Appendix*, Table S2) and align well with the upper volatility trend line, indicating the higher effective volatility of the pure compound. In contrast, when LG is embedded within complex multicomponent mixtures, its apparent volatility shifts markedly toward the lower trend line, demonstrating suppression driven by interactions with coexisting organic species. In addition, recent measurements of LG evaporation from particles of aerosolized mixtures, reporting the ${}^{LG}\Delta H_{vap}$ enthalpy under the assumption that levoglucosan is in the liquid state, suggest that particle size effects and potential phase separation can further influence volatility behavior. These factors lead to lower $\log({}^{LG}C^*_{298\,K})$ values of levoglucosan in aging aerosols, as reflected by the data points and the dashed trend lines reported by Zhang et al. (55). Fig. 2*B* presents the temperature-dependent $\log({}^{LG}C^*_T)$ values calculated using the Clausius–Clapeyron equation and the coupled ${}^{LG}\Delta H^*$ and $\log({}^{LG}C^*_{298\,K})$ values shown in Fig. 2*A*. The intrinsic volatility of p-LG (bright green) remains the highest across the full temperature range. In contrast, the apparent volatility of LG in mixtures is substantially reduced, by up to four orders of magnitude, consistent with strong matrix effects in which intermolecular interactions stabilize LG in the condensed phase and suppress evaporation. The extent of this suppression varies among mixture types, resulting in mixture-specific volatility behavior for LG. This dependence on mixture composition explains the broad clustering of data observed in Fig. 1 and demonstrates that intermolecular interactions within the mixture are key determinants of apparent volatility. Consistent behavior is observed when comparing species with identical elemental composition in laboratory-prepared reference blends (G1 to G4) and in complex wood pyrolysis oil (B1), where species in the complex mixture systematically shift toward the lower-volatility trend (*SI Appendix*, Fig. S5). Collectively, these results confirm that individual species exhibit pronounced, matrix-dependent volatility suppression when present in realistic OA mixtures.

Fig. 3 illustrates the relative importance of compound-specific ($mm_i \times x_i$) and mixture-averaged ($<mm_i \times x_i>$) molecular metrics in explaining variations in ${}^{i}\Delta H^*$ and $\log({}^{i}P^*_{298\,K})$ values, as determined using the gradient boosted machine (GBM) model (*SI Appendix*, Fig. S6) and SHapley Additive exPlanations (SHAP) analysis, where mm_i is one of the molecular metrics and x_i is the relative molar fraction of a component (i). For the SHAP analysis, $\log({}^{i}P^*_{298\,K})$ values were used instead of $\log({}^{i}C^*_{298\,K})$, as vapor pressure is independent of molecular weight and is expressed in units more commonly used in physical chemistry. For both ${}^{i}\Delta H^*$ and $\log({}^{i}P^*_{298\,K})$, mixture-averaged metrics consistently exhibit higher importance than their compound-specific counterparts, indicating that while explicit molecular structure contributes, intermolecular interactions and overall mixture composition play the dominant role in determining apparent volatility. Notably, mixture-averaged molecular metrics show higher relative importance for adequate prediction of both ${}^{i}\Delta H^*$ and $\log({}^{i}P^*_{298\,K})$, with stronger sensitivity observed for ${}^{i}\Delta H^*$. Because ${}^{i}\Delta H^*$ reflects the energetic barrier associated with molecular evaporation, it is inherently influenced by the matrix effects arising from the overall mixture composition. These parameters reflect the bulk physicochemical state of the mixture, including average polarity, hydrogen bonding capacity, and condensed-phase viscosity. In contrast, the corresponding compound-specific descriptors exhibit substantially lower importance, reinforcing that volatility is an emergent property governed more by the mixture matrix than by the intrinsic properties of individual molecules. One apparent exception arises in the SHAP analysis for predicting $\log({}^{i}C^*_{298\,K})$, where compound-specific $MW_i \times x_i$ metric appears as a highly influential feature (*SI Appendix*, Fig. S7).

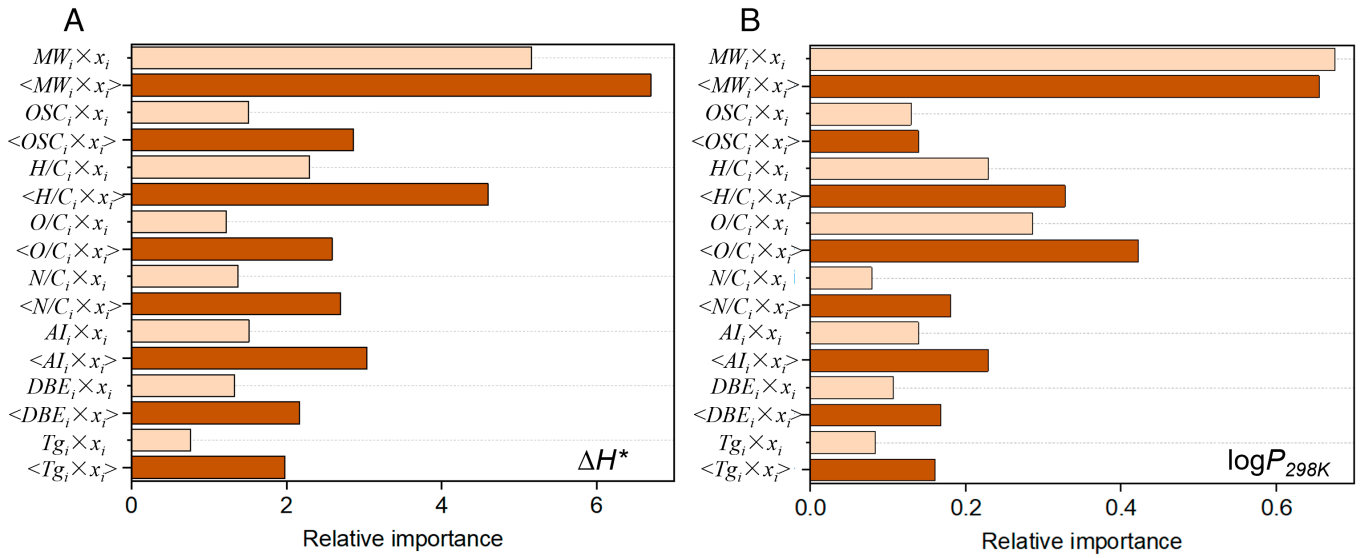

Fig. 3. Global feature importance of compound-specific (light-colored bars) and mixture-averaged (dark-colored bars) molecular metrics for predicting apparent ${}^{i}\Delta H^*$ (*A*) and $\log({}^{i}P^*_{298\,K})$ (*B*) values of individual species, as evaluated using GBM models and SHAP analysis. Light-colored bars represent compound-specific features, expressed as $mm_i \times x_i$, where mm_i is a molecular metric of species (i) and x_i is its relative abundance in the mixture. Dark-colored bars represent mixture-level descriptors, calculated as abundance-weighted averages across all species in a mixture, $< mm_i \times x_i >$. Bar lengths correspond to mean absolute SHAP values averaged over all compound-mixture observations, thereby quantifying the overall contribution of each descriptor to model predictions across the entire dataset. The consistently greater importance of mixture-averaged descriptors indicates that matrix composition exerts a dominant influence on apparent volatility.

This result is expected because compound-specific molecular weight explicitly enters the definition of ${}^{i}C^*_{298\,K}$, whereas mixture-averaged $\langle MW_i \times x_i \rangle$ does not. Consequently, the elevated importance of $MW_i \times x_i$ reflects its numeric role in the ${}^{i}C^*_{298\,K}$ volatility expression rather than a dominant physical control, and it should not be interpreted as evidence that this molecular metric outweighs the matrix effects. Overall, the results in Fig. 3 demonstrate that matrix composition and physical state exert dominant control over apparent volatility, consistent with the volatility suppression and clustering trends observed in Figs. 1 and 2. Accordingly, accurate representation of OA volatility in models requires parameterizations that are mixture-dependent rather than fixed volatility assignments based solely on molecular structures.

Overall, the results presented here demonstrate that the effective volatility of OA components strongly depends on the mixture's properties. Matrix effects related to intermolecular interactions and the elevated viscosity of OA mixtures can suppress apparent volatility by 1 to 4 orders of magnitude, especially in chemically complex and heterogeneous mixtures such as biomass-burning and ambient urban OA. Consequently, volatility parameterizations derived from pure compounds or simplified proxy systems systematically overestimate OA volatility and thus underpredict particle-phase retention and atmospheric lifetimes. Because the aerosol matrix evolves during the TPD ramp as more volatile constituents are progressively removed, the fitted ${}^{i}\Delta H^*$ and $\log({}^{i}C^*_{298\,K})$ values should be interpreted as experimentally derived apparent volatilities that incorporate the effects of changing mixture composition, activity coefficients, viscosity, and mass-transfer limitations. This evolving-matrix behavior is qualitatively consistent with atmospheric OA, whose particle-phase composition continuously adjusts through gas-particle partitioning. Notably, the present measurements were performed under dry-particle conditions; the presence of water may further influence activity coefficients, hydrogen-bonding interactions, viscosity, and mass-transfer processes, making the investigation of humidity-dependent volatility an important direction for future studies.

Inadequate treatment of mixture-dependent volatility suppression can significantly affect WRF-Chem simulations, which are widely used to model pollutant transport, aerosol evolution, and aerosol–cloud–climate interactions. The modeling results presented below illustrate the sensitivity of the WRF-Chem predicted spatial distributions of OA and corresponding cloud condensation nuclei (CCN) across the southeastern United States performed under the default VBS parameterization (59). These default results are compared with scenarios in which the VBS $\log(C^*)$ bins are systematically shifted to lower values by 1, 2, and 3 orders of magnitude, consistent with experimentally observed matrix-induced volatility suppression (Fig. 2*B*). These simulations are not intended to represent the full range of emission sources in the selected region, but rather to demonstrate the sensitivity of WRF-Chem predictions to mixture-dependent volatility suppression. In this sensitivity study, only biomass-burning emissions are considered. The results demonstrate that reduced volatility enhances gas-to-particle partitioning and condensed-phase retention, leading to substantial increases in predicted OA (Fig. 4) and CCN (*SI Appendix*, Fig. S9) under atmospherically relevant conditions.

In the base-case simulation (Fig. 4*A*), OA is widely distributed with the highest mass loadings (~10 to 100 μg m^{-3}) occurring at locations directly influenced by active fire emissions and along their downwind transport pathways. The corresponding CCN number concentrations derived from these OA loadings are on the order of ~10^3 cm^{-3} (*SI Appendix*, Fig. S9*A*), assuming a supersaturation of SS = 0.5% and hygroscopicity parameters of $\kappa = 0.17$ and $\kappa = 0.07$ for biomass burning SOA and POA, respectively (61). Fig. 4 *B–D* show the percent differences in OA mass loadings relative to the base case when the VBS $\log(C^*)$ bins are progressively shifted lower by one, two, and three units, respectively (i.e., reductions in C^* by 1, 2, and 3 orders of magnitude). The corresponding changes in CCN concentrations are presented in *SI Appendix*, Figs. S9 *B–D*. A one-order-of-magnitude reduction in C^* results in modest but widespread increases in OA mass loadings (typically <~60 to 80%), reflecting enhanced particle-phase partitioning of semivolatile species. Reducing volatility by two

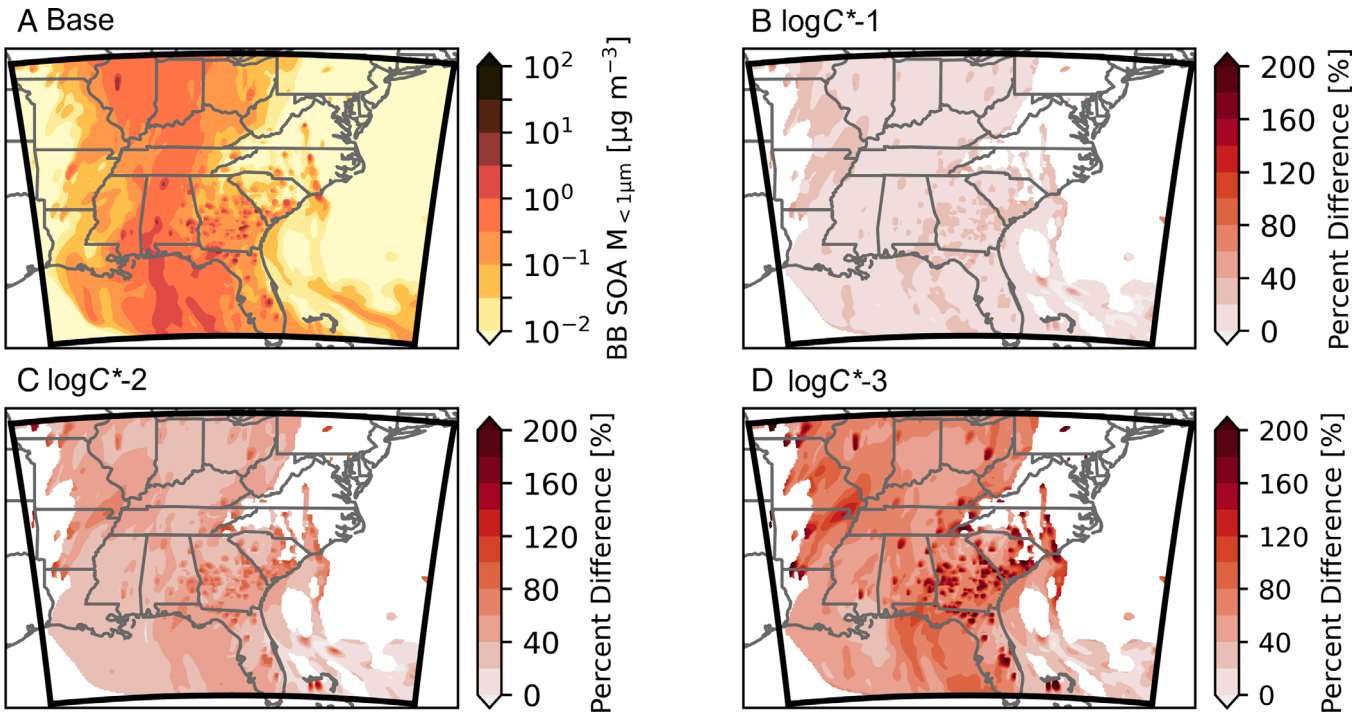

Fig. 4. WRF-Chem–simulated mass loadings of submicron biomass-burning (BB) SOA across the southeastern United States modeling domain on March 18, 2025, at 20 UTC, using the QFED fire emissions dataset, the hotspots represent locations of local fires (60). (*A*) Base-case simulation employing the default VBS distribution. (*B–D*) Percent differences in OA mass loadings relative to the base case for simulations in which the VBS log*C** bins are shifted lower by one-, two-, and three-unit values, respectively. The percent difference is calculated above a BB SOA concentration threshold of 10^{-2} µg m^{-3}.

orders of magnitude produces substantially larger increases, exceeding 100% across broad portions of the domain. The strongest response occurs when *C** values are reduced by three orders of magnitude, producing widespread enhancements exceeding 100% and localized increases exceeding 200%, particularly in regions directly influenced by wildfire emissions and along major transport pathways. The corresponding increases in CCN concentrations are ~15%, ~30%, and ~60%, respectively. Consistent sensitivity of WRF-Chem modeling predictions is observed in simulations for March 19, 2025 (*SI Appendix*, Figs. S8–S10), which likewise show strong responses of OA and CCN to volatility suppression. The magnitude and spatial extent of OA and CCN enhancements increase as volatility decreases, with particularly pronounced responses in regions influenced by aged and transported plumes. The stronger response observed on March 19 reflects the cumulative effects of atmospheric transport and aging, which allow semivolatile species more time to repartition into the condensed phase when volatility is reduced. The projected ~15 to 60% increases in CCN concentrations are large enough to significantly alter cloud microphysics, leading to higher droplet number concentrations, smaller droplet sizes, longer cloud lifetimes, and enhanced cloud reflectivity.

Atmospheric Impacts. These results demonstrate that matrix-induced volatility suppression, as observed experimentally, can substantially increase predicted OA mass loadings and CCN concentrations across both near-source and downwind regions, particularly with biomass-burning plumes. They further indicate that VBS parameterizations derived from pure compounds or simplified proxy mixtures likely overestimate volatility and underestimate particle-phase retention and atmospheric persistence. Incorporating mixture-dependent volatility parameterizations into chemical transport models is therefore essential for improving predictions of OA mass loadings, phase state, spatial distributions, aging transformations, and atmospheric impacts.

The strong increases in OA mass loadings projected under suppressed-volatility scenarios also highlight broader atmospheric implications. Enhanced particle-phase retention increases OA lifetime and facilitates the long-range transport of biomass-burning signatures, potentially elevating regional background organic aerosol concentrations far from source regions. Because particle-phase enrichment increases aerosol absorption and stabilizes light-absorbing chromophores (62), mixture-suppressed volatility may amplify the radiative influence of brown carbon compared to model predictions based solely on intrinsic volatilities. The spatially extensive OA and CCN enhancements further imply stronger aerosol–cloud interactions through increased particle sizes and altered hygroscopic growth, with potential consequences for cloud activation and lifetimes, boundary-layer dynamics, and regional radiative forcing.

From an air-quality perspective, these results suggest that chemical transport models relying on volatility parameters derived from pure compounds likely underestimate $PM_{2.5}$ burdens during wildfire events, especially in aging-dominated regions downwind. Such biases can propagate into public-health assessments and visibility predictions. Accounting for mixture-dependent volatility is therefore essential not only for closing long standing model-measurement gaps but also for improving regional exposure assessment under various atmospheric pollution scenarios.

Materials and Methods

Sample Details. This work combines temperature-dependent volatility datasets summarizing measurements for 33 mixtures collected in laboratory experiments, test-facility studies, field campaigns, as well as selected mixtures of reference organic compounds. A summary list of mixtures, sample identifiers, and their sources is provided in *SI Appendix*, Table S1. The datasets include: laboratory-generated SOA proxy mixtures (S samples) (36, 37, 39); reference mixtures of selected organic compounds commonly associated with biomass-burning

emissions (G samples) (63); commercial e-cigarette liquids (E samples); laboratory-generated biomass-burning OA proxies (B samples) (38); ambient OA samples collected in a field study (A samples) (40); and OA mixtures produced in pyrolysis experiments with commercial construction materials, including structural wood (W samples), fiberboard (F samples), and plastics (P samples) (64, 65).

HRMS Measurements and Data analysis. The ${}^{i}\Delta H^{*}$ and $\log({}^{i}C^{*}_{298\,K})$ values for individual species in each mixture were obtained from TPD–DART–HRMS measurements, with the instrumental setup, operating procedures, and data-analysis workflow described in detail elsewhere (36, 37) and also summarized in *SI Appendix*, Supplementary Note 1. Briefly, filter-collected samples (S, A, W, F, P) were sectioned and mounted onto a copper stub nested within the TPD heating block, whereas condensate samples (G, E, B) were pipetted (~6 μL) directly into the well at the center of the copper stub. The TPD ramping profile started at 298 K, held for 0.4 min, followed by a linear ramp at a rate of 70 K min^{-1} to 623 K, and then maintained at the final temperature for 2 min. The DART ionization source, interfaced with the Q-Exactive HF-X Orbitrap mass analyzer (operated at mass resolution of m/Δm ~240,000 at 200 m/z), dynamically ionized the gas-phase species degassing from the analyzed samples during the TPD experimental runs. Progression of the high-resolution mass spectra was recorded to identify individual components and construct their corresponding extracted ion thermograms. Molecular formulas were assigned based on the ions detected in negative mode, (–)DART–HRMS in the m/z range of 100 to 1,000 Da, with constraints of $C_{1\text{-}40}H_{1\text{-}100}O_{1\text{-}25}N_{0\text{-}1}$ and mass tolerance of ± 2.0 ppm (66). The (–) DART ionization mechanism yields mostly ions of deprotonated molecules $[M-H]^{-}$ and occasional radical anions $M^{-\bullet}$. Extracted ion thermograms for each species were used to obtain the apparent ${}^{i}\Delta H^{*}$ and $\log({}^{i}C^{*}_{298\,K})$ values, capturing the effective volatility (reported as either ${}^{i}C^{*}_{T}$, μg·m^{-3} or p^{*}_{T}, Pa) of each compound as expressed within the specific mixture analyzed (36, 37).

Molecular Metrics Calculations. Characteristic molecular metrics (*mm*) were calculated for each neutral molecular species (*i*), including molecular weight (*MW*), carbon oxidation state (OS_C), elemental ratios (*H/C, O/C, N/C*), modified aromaticity index (*AI*), double bond equivalent (*DBE*), and component-specific glass transition temperature (T_g). Equations (67–70) used for the calculations of mm_i values are summarized in *SI Appendix*, Supplementary Note 1. Mole fractions (x_i) of the individual species were approximated as $x_i = h_i/h_{total}$, where h_i is the integrated area of the single ion thermogram for species *i* and h_{total} is the integrated area of the total negative ion thermogram of all successfully identified species, under the operational assumption that ion signal scales with concentration with more than 70% total organic aerosol mass. Although this assumption implies uniform ionization efficiency across all detected species, which is an oversimplification, it provides practical numerical values of x_i that serve as proxies for true mole fractions and can be consistently used in the machine learning modeling framework described below.

SHAP Model Analysis. To assess the relative influence of compound-specific versus mixture-dependent properties, we use the products of $mm_i \times x_i$ to describe individual species and their mixture-averaged values $<mm_i \times x_i>$ to represent each analyzed mixture as a whole, where *mm* corresponds to any of the molecular metrics listed above. Complete list of the individual species, their ${}^{i}\Delta H^{*}$, $\log({}^{i}C^{*}_{298\,K})$, $mm_i \times x_i$, and $<mm_i \times x_i>$ values reported in this study are provided in Dataset S1. The best-performing GBM model was retained and used for the subsequent machine learning feature-attribution analysis (71). Mean absolute SHAP was used to rank feature importance for predicting ${}^{i}\Delta H^{*}$ and $\log({}^{i}p^{*}_{298\,K})$, respectively. SHAP values, rooted in cooperative game theory (72), provide a unified framework to quantify how each feature contributes to the deviation of a model's prediction, calculated with all features included, from the mean prediction averaged across all possible feature subsets (73, 74). SHAP analysis was performed in R software (version 4.3.3). Performance summaries of the models for the two volatility targets are shown in *SI Appendix*, Table S3 and Fig. S6. For each fitted model, SHAP values were computed for all compounds, and the mean absolute SHAP values were used to rank the relative importance of the molecular metrics. This approach provides an interpretable and quantitative framework for assessing nonlinear relationships and interactions among molecular compositional features. A detailed description of the SHAP analysis is presented in *SI Appendix*, Supplementary Note 3.

WRF-Chem Atmospheric Simulations. WRF-Chem (version 4.2) simulations were conducted at 12 km horizontal resolution for a domain over the southeastern United States for March 16–19, 2025 with March 15 being used to spin-up the meteorological and chemical conditions. The gas-phase and aerosol phase chemistry used in these simulations has been described in detail in Shrivastava et al. (60). In all WRF-Chem simulations, the BB emissions of trace gases and primary particles were inferred from the Quick Fire Emissions Database (QFED), while emissions of BB SOA precursors were determined based on their emissions ratio with CO as documented in footnote of *SI Appendix*, Table S4 (75, 76). For computational efficiency, BB POA is represented by a single semivolatile species with a C^{*} of 1 μg m^{-3}. Volatile BB SOA precursors are represented in two classes: oxygenated aromatics and other (e.g., furans, aromatic hydrocarbons, acyclic VOCs, and monoterpenes). In the base case, the BB SOA precursors react with OH to form SOA in a 4 bin VBS with C^{*} of 0.01, 1, 100, and 10,000 μg m^{-3} with the relative mass fractions in each bin depending on SOA class (*SI Appendix*, Table S4) (59), followed by further multigenerational aging of these precursors. To assess the sensitivity of WRF-Chem predictions to lower volatility, three simulations were conducted which shift the original BB SOA VBS 1, 2, and 3 orders of magnitude lower. All other aspects of the WRF-Chem simulations are consistent between the base case and the sensitivity simulations. Underlying hygroscopicity assumptions for estimating CCN concentrations, along with additional details of WRF-Chem simulations, are provided in *SI Appendix*, Supplementary Note 4.

Data, Materials, and Software Availability. All study data are included in the article and/or supporting information.

ACKNOWLEDGMENTS. The Purdue University group acknowledges support from the U.S. National Oceanic and Atmospheric Administration Grant NA22OAR4310195. The University of California, Irvine group acknowledges support from the U.S. National Oceanic and Atmospheric Administration Grant NA22OAR4310196. MS and NJ were supported by the U.S. Department of Energy (DOE) Office of Science, Office of Biological and Environmental Research through the Atmospheric System Research program. Computational resources for the Weather Research and Forecasting model coupled with Chemistry (WRF-Chem) simulations were provided by Environmental Molecular Sciences Laboratory [a DOE Office of Science User Facility sponsored by the Office of Biological and Environmental Research located at Pacific Northwest National Laboratory (PNNL)] and the PNNL Institutional Computing facility. The PNNL is operated for DOE by Battelle Memorial Institute under Contract DE-AC06-76RL01830. K.R., C.L., and S.H.J. were supported by the Atmospheric Chemistry, Carbon Cycle and Climate program at the National Oceanic and Atmospheric Administration (NA22OAR4310537) and by the Atmosphere Cluster program at the NSF (AGS-2519789). Y.R. acknowledges support from the European Union's Horizon Europe (2021–2027) research and innovation program under project EASVOLEE (Grant Agreement No. 101095457). We thank Dr. V. Moschos and Prof. J. Surratt from the University of North Carolina for providing mixtures of brown carbon reference compounds.

Author affiliations: [a]Department of Chemistry, Purdue University, West Lafayette, IN 47907; [b]Knell Family Institute for Artificial Intelligence, Weizmann Institute of Science, Rehovot 76100, Israel; [c]Atmospheric, Climate, and Earth Sciences Division, Pacific Northwest National Laboratory, Richland, WA 99352; [d]School of Geography, Earth and Environmental Science, University of Birmingham, Birmingham B15 2TT, United Kingdom; [e]Department of Mechanical Engineering, Colorado State University, Fort Collins, CO 80523; [f]Department of Chemistry, University of California, Irvine, CA 92697; [g]Department of Earth and Planetary Sciences, Faculty of Chemistry, Weizmann Institute of Science, Rehovot 76100, Israel; and [h]Department of Earth, Atmospheric, and Planetary Sciences, Purdue University, West Lafayette, IN 47907

1. D. Bhattu, "Primary organic aerosols" in *Air Pollution and Control*, N. Sharma, A. K. Agarwal, P. Eastwood, T. Gupta, A. P. Singh, Eds. (Springer Singapore, Singapore, 2018), pp. 109–117.
2. B. B. Palm *et al.*, Quantification of organic aerosol and brown carbon evolution in fresh wildfire plumes. *Proc. Natl. Acad. Sci. U.S.A.* **117**, 29469–29477 (2020).
3. J. De Gouw, J. L. Jimenez, Organic aerosols in the Earth's atmosphere. *Environ. Sci. Technol.* **43**, 7614–7618 (2009).
4. M. Hallquist *et al.*, The formation, properties and impact of secondary organic aerosol: Current and emerging issues. *Atmos. Chem. Phys.* **9**, 5155–5236 (2009).
5. M. Mahilang, M. K. Deb, S. Pervez, Biogenic secondary organic aerosols: A review on formation mechanism, analytical challenges and environmental impacts. *Chemosphere* **262**, 127771 (2021).
6. M. O. Andreae, A. Gelencsér, Black carbon or brown carbon? The nature of light-absorbing carbonaceous aerosols. *Atmos. Chem. Phys.* **6**, 3131–3148 (2006).

7. C. George, M. Ammann, B. D'Anna, D. J. Donaldson, S. A. Nizkorodov, Heterogeneous photochemistry in the atmosphere. *Chem. Rev.* **115**, 4218–4258 (2015).
8. T. Moise, J. M. Flores, Y. Rudich, Optical properties of secondary organic aerosols and their changes by chemical processes. *Chem. Rev.* **115**, 4400–4439 (2015).
9. A. Laskin, J. Laskin, S. A. Nizkorodov, Chemistry of atmospheric brown carbon. *Chem. Rev.* **115**, 4335–4382 (2015).
10. D. K. Farmer, C. D. Cappa, S. M. Kreidenweis, Atmospheric processes and their controlling influence on cloud condensation nuclei activity. *Chem. Rev.* **115**, 4199–4217 (2015).
11. H. Herrmann *et al.*, Tropospheric aqueous-phase chemistry: Kinetics, mechanisms, and its coupling to a changing gas phase. *Chem. Rev.* **115**, 4259–4334 (2015).
12. W. Li *et al.*, Aqueous-phase secondary organic aerosol formation on mineral dust. *Natl. Sci. Rev.* **12**, nwaf221 (2025).
13. M. J. Rogers *et al.*, Humid summers promote urban aqueous-phase production of oxygenated organic aerosol in the Northeastern United States. *Geophys. Res. Lett.* **52**, e2024GL112005 (2025).
14. M. Shrivastava *et al.*, Recent advances in understanding secondary organic aerosol: Implications for global climate forcing. *Rev. Geophys.* **55**, 509–559 (2017).
15. N. M. Donahue, J. H. Kroll, S. N. Pandis, A. L. Robinson, A two-dimensional volatility basis set–Part 2: Diagnostics of organic-aerosol evolution. *Atmos. Chem. Phys.* **12**, 615–634 (2012).
16. G. Isaacman-VanWertz *et al.*, Chemical evolution of atmospheric organic carbon over multiple generations of oxidation. *Nat. Chem.* **10**, 462–468 (2018).
17. X. Zhang *et al.*, Formation and evolution of molecular products in α-pinene secondary organic aerosol. *Proc. Natl. Acad. Sci. U.S.A.* **112**, 14168–14173 (2015).
18. J. Tröstl *et al.*, The role of low-volatility organic compounds in initial particle growth in the atmosphere. *Nature* **533**, 527 (2016).
19. A. L. Vogel, J. Schneider, C. Muller-Tautges, T. Klimach, T. Hoffmann, Aerosol chemistry resolved by mass spectrometry: Insights into particle growth after ambient new particle formation. *Environ. Sci. Technol.* **50**, 10814–10822 (2016).
20. J. F. Pankow, W. E. Asher, SIMPOL.1: A simple group contribution method for predicting vapor pressures and enthalpies of vaporization of multifunctional organic compounds. *Atmos. Chem. Phys.* **8**, 2773–2796 (2008).
21. D. A. Amaladhasan *et al.*, Modelling the gas-particle partitioning and water uptake of isoprene-derived secondary organic aerosol at high and low relative humidity. *Atmos. Chem. Phys.* **22**, 215–244 (2022).
22. W. Huang *et al.*, Variation in chemical composition and volatility of oxygenated organic aerosol in different rural, urban, and mountain environments. *Atmos. Chem. Phys.* **24**, 2607–2624 (2024).
23. X. Chang *et al.*, Full-volatility emission framework corrects missing and underestimated secondary organic aerosol sources. *One Earth* **5**, 403–412 (2022).
24. D. L. Ortiz-Montalvo *et al.*, Ammonium addition (and aerosol pH) has a dramatic impact on the volatility and yield of glyoxal secondary organic aerosol. *Environ. Sci. Technol.* **48**, 255–262 (2014).
25. F. D. Lopez-Hilfiker *et al.*, Molecular composition and volatility of organic aerosol in the Southeastern US: Implications for IEPOX derived SOA. *Environ. Sci. Technol.* **50**, 2200–2209 (2016).
26. Q. Ye *et al.*, Molecular composition and volatility of nucleated particles from α-Pinene oxidation between -50 °C and +25 °C. *Environ. Sci. Technol.* **53**, 12357–12365 (2019).
27. L. Y. Gao *et al.*, Volatility of secondary organic aerosol from β-caryophyllene ozonolysis over a wide tropospheric temperature range. *Environ. Sci. Technol.* **57**, 8965–8974 (2023).
28. M. Surdu *et al.*, Molecular understanding of the enhancement in organic aerosol mass at high relative humidity. *Environ. Sci. Technol.* **57**, 2297–2309 (2023).
29. K. P. Cain, E. Karnezi, S. N. Pandis, Challenges in determining atmospheric organic aerosol volatility distributions using thermal evaporation techniques. *Aerosol Sci. Technol.* **54**, 941–957 (2020).
30. B. Jiang *et al.*, Intrinsic chemical drivers of organic aerosol volatility: From experimental insights to model predictions. *J. Geophys. Res.: Atmos.* **129**, e2024JD041286 (2024).
31. W. Chen *et al.*, Quantitative characterization of the volatility distribution of organic aerosols in a polluted urban area: Intercomparison between thermodenuder and molecular measurements. *J. Geophys. Res.: Atmos.* **129**, e2023JD040284 (2024).
32. N. M. Donahue, S. A. Epstein, S. N. Pandis, A. L. Robinson, A two-dimensional volatility basis set: 1. Organic-aerosol mixing thermodynamics. *Atmos. Chem. Phys.* **11**, 3303–3318 (2011).
33. C. Mohr *et al.*, Molecular identification of organic vapors driving atmospheric nanoparticle growth. *Nat. Commun.* **10**, 1–7 (2019).
34. W. Nie *et al.*, Secondary organic aerosol formed by condensing anthropogenic vapours over China's megacities. *Nat. Geosci.* **15**, 255–261 (2022).
35. Y. Li, U. Poeschl, M. Shiraiwa, Molecular corridors and parameterizations of volatility in the chemical evolution of organic aerosols. *Atmos. Chem. Phys.* **16**, 3327–3344 (2016).
36. C. P. West *et al.*, Volatility measurements of individual components in organic aerosol mixtures using temperature-programmed desorption–direct analysis in real time–high resolution mass spectrometry. *Anal. Chem.* **95**, 7403–7408 (2023).
37. Q. Xie *et al.*, Volatility basis set distributions and viscosity of organic aerosol mixtures: Insights from chemical characterization using temperature-programmed desorption-direct analysis in real-time high-resolution mass spectrometry. *Anal. Chem.* **96**, 9524–9534 (2024).
38. Q. Xie *et al.*, Molecular insights into gas–particle partitioning and viscosity of atmospheric brown carbon. *Environ. Sci. Technol.* **58**, 18284–18294 (2024).
39. Q. Xie *et al.*, Distinct gas–particle partitioning and viscosity characteristics of secondary organic aerosols derived from α-pinene versus ocimene. *ACS ES&T-Air* **2**, 1916–1926 (2025).
40. Q. Xie *et al.*, Molecular characterization of composition and volatility of ambient organic aerosol sampled by an UAV-mounted portable aethalometer. *Anal. Chem.* **97**, 17743–17751 (2025).
41. T. D. Vaden, D. Imre, J. Beranek, M. Shrivastava, A. Zelenyuk, Evaporation kinetics and phase of laboratory and ambient secondary organic aerosol. *Proc. Natl. Acad. Sci. U.S.A.* **108**, 2190–2195 (2011).
42. J. Wilson, D. Imre, J. Beranek, M. Shrivastava, A. Zelenyuk, Evaporation kinetics of laboratory-generated secondary organic aerosols at elevated relative humidity. *Environ. Sci. Technol.* **49**, 243–249 (2015).
43. L. Renbaum-Wolff *et al.*, Viscosity of alpha-pinene secondary organic material and implications for particle growth and reactivity. *Proc. Natl. Acad. Sci. U.S.A.* **110**, 8014–8019 (2013).
44. C. Kidd, V. Perraud, L. M. Wingen, B. J. Finlayson-Pitts, Integrating phase and composition of secondary organic aerosol from the ozonolysis of alpha-pinene. *Proc. Natl. Acad. Sci. U.S.A.* **111**, 7552–7557 (2014).
45. A. P. Bateman, A. K. Bertram, S. T. Martin, Hygroscopic influence on the semisolid-to-liquid transition of secondary organic materials. *J. Phys. Chem. A* **119**, 4386–4395 (2015).
46. Y. Zhang *et al.*, Changing shapes and implied viscosities of suspended submicron particles. *Atmos. Chem. Phys.* **15**, 7819–7829 (2015).
47. J. W. Grayson *et al.*, Effect of varying experimental conditions on the viscosity of α-pinene derived secondary organic material. *Atmos. Chem. Phys.* **16**, 6027–6040 (2016).
48. A. A. May *et al.*, Gas-particle partitioning of primary organic aerosol emissions: 3. Biomass burning. *J. Geophys. Res. Atmos.* **118**, 11327–11338 (2013).
49. S. A. Epstein, I. Riipinen, N. M. Donahue, A semiempirical correlation between enthalpy of vaporization and saturation concentration for organic aerosol. *Environ. Sci. Technol.* **44**, 743–748 (2010).
50. M. Ranjan, A. A. Presto, A. A. May, A. L. Robinson, Temperature dependence of gas–particle partitioning of primary organic aerosol emissions from a small diesel engine. *Aerosol Sci. Technol.* **46**, 13–21 (2012).
51. V. Besel, M. Todorović, T. Kurtén, P. Rinke, H. Vehkamäki, Atomic structures, conformers and thermodynamic properties of 32k atmospheric molecules. *Sci. Data* **10**, 450 (2023).
52. J. Ferraz-Caetano, F. Teixeira, M. N. D. S. Cordeiro, Data-driven, explainable machine learning model for predicting volatile organic compounds' standard vaporization enthalpy. *Chemosphere* **359**, 142257 (2024).
53. Y. Li *et al.*, Impacts of chemical degradation on the global budget of atmospheric levoglucosan and its use as a biomass burning tracer. *Environ. Sci. Technol.* **55**, 5525–5536 (2021).
54. B. R. Simoneit *et al.*, Levoglucosan, a tracer for cellulose in biomass burning and atmospheric particles. *Atmos. Environ.* **33**, 173–182 (1999).
55. J. Zhang *et al.*, Estimation of the volatility and apparent activity coefficient of levoglucosan in wood-burning organic aerosols. *Environ. Sci. Technol. Lett.* **11**, 1214–1219 (2024).
56. V. Oja, E. M. Suuberg, Vapor pressures and enthalpies of sublimation of d-glucose, d-xylose, cellobiose, and levoglucosan. *J. Chem. Eng. Data* **44**, 26–29 (1999).
57. A. M. Booth *et al.*, Solid state and sub-cooled liquid vapour pressures of cyclic aliphatic dicarboxylic acids. *Atmos. Chem. Phys.* **11**, 655–665 (2011).
58. A. A. May, R. Saleh, C. J. Hennigan, N. M. Donahue, A. L. Robinson, Volatility of organic molecular markers used for source apportionment analysis: Measurements and implications for atmospheric lifetime. *Environ. Sci. Technol.* **46**, 12435–12444 (2012).
59. M. Shrivastava *et al.*, Intense formation of secondary ultrafine particles from Amazonian vegetation fires and their invigoration of deep clouds and precipitation. *One Earth* **7**, 1029–1043 (2024).
60. M. Shrivastava *et al.*, Anthropogenic extremely low volatility organics (ELVOCs) govern the growth of molecular clusters over the southern great plains during the springtime. *J. Geophys. Res.-Atmos.* **129**, e2024JD041212 (2024).
61. A. Bougiatioti *et al.*, Biomass-burning impact on CCN number, hygroscopicity and cloud formation during summertime in the eastern Mediterranean. *Atmos. Chem. Phys.* **16**, 7389–7409 (2016).
62. D. Calderon-Arrieta *et al.*, Enhanced light absorption and elevated viscosity of atmospheric brown carbon through evaporation of volatile components. *Environ. Sci. Technol.* **58**, 7493–7504 (2024).
63. V. Moschos *et al.*, Quantifying the light-absorption properties and molecular composition of brown carbon aerosol from sub-Saharan African biomass combustion. *Environ. Sci. Technol.* **58**, 4268–4280 (2024).
64. K. S. Hopstock *et al.*, Molecular characterization and photoreactivity of organic aerosols formed from pyrolysis of urban materials during fires at the wildland-urban interface. *ACS ES&T Air* **1**, 1495–1506 (2024).
65. K. Ridgway *et al.*, Emissions from structure fires: Overview of BHASMA and results for CO_2 and select pollutants by fuel, combustion mode, and scale. *Environ. Sci. Technol.* **59**, 23926–23937 (2025).
66. P. J. Roach, J. Laskin, A. Laskin, Higher-order mass defect analysis for mass spectra of complex organic mixtures. *Anal. Chem.* **83**, 4924–4929 (2011).
67. F. W. McLafferty, F. Turecek, *Interpretation of Mass Spectra* (University Science Books, ed. 4, 1993), p. 371.
68. B. P. Koch, T. Dittmar, From mass to structure: An aromaticity index for high-resolution mass data of natural organic matter. *Rapid Commun. Mass Spectrom.* **30**, 250–250 (2016).
69. W. S. W. DeRieux *et al.*, Predicting the glass transition temperature and viscosity of secondary organic material using molecular composition. *Atmos. Chem. Phys.* **18**, 6331–6351 (2018).
70. J. H. Kroll *et al.*, Carbon oxidation state as a metric for describing the chemistry of atmospheric organic aerosol. *Nat. Chem.* **3**, 133–139 (2011).
71. J. H. Friedman, Greedy function approximation: A gradient boosting machine. *Ann. Stat.* **29**, 1189–1232 (2001).
72. L. S. Shapley, Stochastic games. *Proc. Natl. Acad. Sci. U.S.A.* **39**, 1095–1100 (1953).
73. S. M. Lundberg, S.-I. Lee, A unified approach to interpreting model predictions. *Adv. Neural Inf. Process. Syst.* **30**, 4765–4774 (2017).
74. S. M. Lundberg *et al.*, From local explanations to global understanding with explainable AI for trees. *Nat. Mach. Intell.* **2**, 56–67 (2020).
75. R. D. Koster, A. S. Darmenov, A. M. da Silva, The Quick Fire Emissions Dataset (QFED): Documentation of Versions 2.1, 2.2 and 2.4: Technical Report series on global modeling and data assimilation–Volume 38. NASA Technical Memorandum 5253 (Tech. Rep., 2015).
76. R. D. Koster *et al.*, "Technical report series on global modeling and data assimilation, Volume 41: GDIS Workshop Report" (Tech. Rep., 2015).